Rotational State Selection and Orientation of OH and OD Radicals by Electric Hexapole Beam-Focusing

Toby D. Hain,[†] Michael A. Weibel,[‡] Kyle M. Backstrand,[§] and Thomas J. Curtiss*,[||]

Department of Chemistry, University of Utah, Salt Lake City, Utah 84112

Received: April 15, 1997; In Final Form: June 23, 1997[⊗]

An electrostatic hexapole was used to state-select OH and OD radicals in single, low-lying, $|J\Omega M_J\rangle$ rotational states. The radicals were produced in a corona discharge, supersonic molecular beam source by dissociating H_2O (D_2O) seeded in Ar or He. Beam velocities ranged from 650 to 1850 m s^{-1}, and translational temperatures were less than 10 K for all expansion conditions. Measured beam flux densities, J, of selected states were high (e.g., J > 10^{13} radicals cm^{-2} s^{-1} for the $|^3/_2\ \pm^3/_2\ \mp^3/_2\rangle$ states of OH seeded in He). Classical trajectory simulations reproduced the well-resolved rotational state structure of experimental beam-focusing spectra. Simulations were based on a Stark energy analysis of the rotational energy levels, including significant effects due to Λ-doubling and spin−orbit coupling. Orientational probability distribution functions were calculated in the high-field limit for all selectable states and demonstrate exceptional experimental control over collision geometry for scattering experiments.

1. Introduction

The hydroxyl radical plays a major role in many chemistries including atmospheric, combustion, catalytic, and interstellar. In combustion, it is involved in the conversion of CO to CO_2[1] among many other hydrocarbon oxidation steps.[2,3] In the atmosphere, hydrogen abstraction by hydroxyl radicals is ubiquitous. In the troposphere, hydrogen abstraction by OH is the primary removal process for alkanes[4] and partially halogenated hydrocarbons[5] as well as the main route to hydrocarbon radical formation.[6] The OH reaction with dimethyl sulfide (DMS) is the principal sulfur loss mechanism in marine boundary layers.[7] In the stratosphere, the OH radical is a key participant in a catalytic cycle responsible for 30−50% of O_3 losses.[8] The hydroxyl radical's role in the catalytic oxidation of hydrogen to form H_2O on transition metal surfaces has been the focus of recent interest.[9−12] It has also been suggested that OH is an important plasma-surface species for hydrogen terminated surfaces.[13] The OH radical has been one of the most well-studied radicals in the investigation of interstellar masers.[14] Beyond the arena of masers, interstellar OH, reacting with H_2, is responsible for cosmic water formation.[15]

In recent years, the reaction dynamics of the four-atom OH + H_2 → H_2O + H reaction has also been the subject of experimental studies[16] and extensive theoretical scattering dynamics investigations.[17] Of particular interest in the context of the orientational control we have over collision geometry are the time-dependent wave-packet studies of Zhang and Zhang.[18] These suggest that strong steric effects should be seen for this system. Also the subject of recent scattering calculations have been studies of OH + CH_4 → H_2O + CH_3,[19] OH + HCl → H_2O + Cl,[20] and OH + NH_3 → H_2O + NH_2.[21] No experimental reactive scattering dynamics studies for the latter three systems have been undertaken.

Due to the broad ranging importance of OH radical reactions and the growing theoretical attention being given to them, we have developed an exceptional beam source of hydroxyl radicals. Our purpose was to develop the optimal radical beam source for advanced experimental studies in gas phase and surface molecular dynamics. Radicals are state-selected and oriented, and the radical beam is purified and intensified by the unique focusing properties of an electrostatic hexapole. In this paper we fully describe measurements and trajectory simulations that characterize our new hydroxyl radical source.

The rest of this paper is divided into five sections. In the next section, the molecular beam apparatus is fully described for the first time. The experimental determination of beam intensities and velocities is also given. An exposition of electric field deflection, Stark energy calculations, and the computer algorithms used for trajectory simulations is provided in section 3. The fourth section presents experimental and simulated results of beam-focusing studies. In section 5, we discuss the orientational character of state-selected OH/OD beams. Finally, we close with a summary of the preceding sections.

2. Experimental Section

The design of our molecular beam machine has been briefly outlined in previous publications[22,23] and will now be fully described. Figure 1 shows a scale drawing of the apparatus, and Table 1 provides critical dimensions.

The beam line consists of four regions (source, chopper, hexapole, and detection) separately pumped by diffusion pumps. The source region contains a corona discharge beam source.[24] The source nozzle is fabricated from a 12 mm o.d. heavy-walled quartz tube that is drawn down and sealed off. The sealed end is cut off and sanded back until a 50−100 μm diameter aperture is created. The anode of the discharge consists of a sharpened 0.5 mm diameter platinum wire that terminates approximately 1 mm from the nozzle aperture. A rare gas/water vapor mixture is produced by bubbling the rare gas through liquid water at room temperature at a total pressure of approximately 1600 Torr. The resulting gas mixture (ca. 1% water) expands out of the nozzle, and electron current counterpropagates through the expanding gas from the grounded skimmer to the positively biased anode, creating a sustained glow discharge.

A conical Monel skimmer with a 1.5 mm diameter aperture separates the source and chopper regions. The chopper region houses a motor driven chopper wheel that modulates the beam

[†] E-mail address: tdhain@atlas.chem.utah.edu.
[‡] E-mail address: weibel@atlas.chem.utah.edu.
[§] E-mail address: backstrand@atlas.chem.utah.edu.
[||] E-mail address: curtiss@atlas.chem.utah.edu.
[⊗] Abstract published in *Advance ACS Abstracts,* September 15, 1997.

S1089-5639(97)01299-1 CCC: $14.00

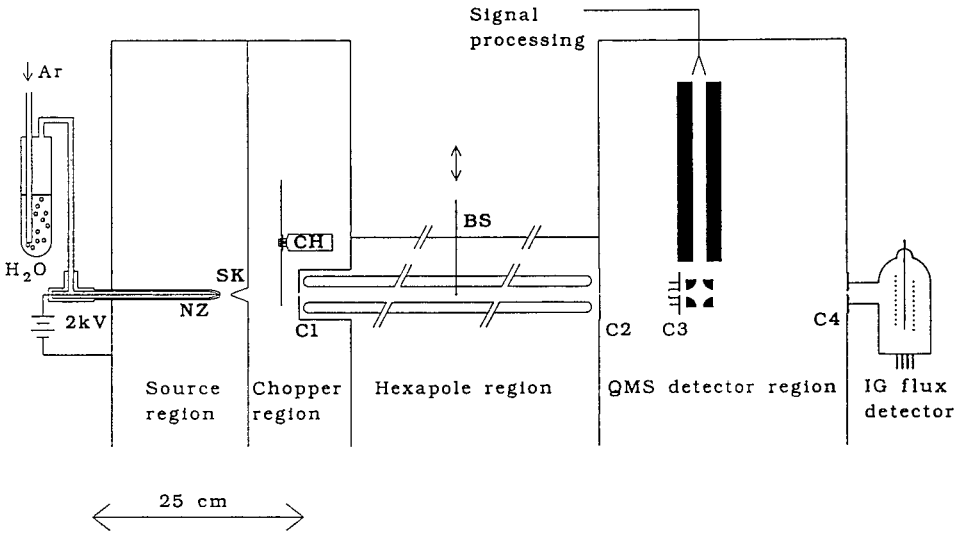

Figure 1. Diagram drawn to scale of the hexapole beam machine. The hexapoles and hexapole chamber have been shortened to accommodate the entire machine in the frame. Argon gas is bubbled through a bath of water to create a gas mixture rich in H_2O vapor. This mixture expands out of the nozzle (NZ) into the source region. Electrons from the grounded skimmer (SK) are accelerated through the gas, generating a glow discharge. The beam is modulated with a rotating chopper wheel (CH) in the chopper region before passing through the first collimator (C1) into the hexapole region. An electrostatic hexapole focuses OH radicals around a beam stop (BS) located near the center of the beam line. Nonfocused species are removed by the beam stop while focused OH enters the QMS detector region through the second collimator (C2). OH radicals are further collimated with a large diameter collimator on the QMS (C3). Ions formed in the ionizer of the QMS are turned with a turning quadrupole and mass selected with another quadrupole. Beam fluxes are measured with an ion gauge accumulation detector, which is separated from the QMS region with a fourth collimator (C4).

TABLE 1: Instrumental Parameters[a]

distance from nozzle aperture	distance (cm)	radius (mm)
nozzle (aperture)	0	0.03
skimmer (aperture)	1.0	0.75
chopper wheel	7.0	0.81,[b] 76[c]
C1 (source side face)	9.0	3.40
start of hexapole	9.6	9.6[d]
beam stop	110.0	1.27
end of hexapole	202.7	9.6[d]
C2 (source side face)	203.6	0.76
C3	211.7	2.38
ionizer filaments	212.3	N/A
C4	233.8	1.72

[a] Distances from the nozzle aperture and various parts of the beam machine as well as radii of the components are tabulated. Note collimators C1 and C2 have finite thicknesses with the distance meaured as notated in parentheses. [b] Time-of-flight slit width. [c] Radius from center. [d] See ref 25.

for phase-sensitive detection and for time-of-flight velocity measurements. The 15.2 cm diameter wheel was etched with photolithography (Fotofabrication Corp., Chicago) to produce five separate hole patterns that can access the beam by translating the chopper. The two patterns used in the studies described here were a 50% on−off pattern for beam detection using a lock-in amplifier and a pattern with two 0.81 mm wide slits 180° apart on the wheel for time-of-flight measurements. The wheel speed was typically 100 Hz, and the period of rotation was constant to within 0.2%. Velocity measurements are described below.

A 3.4 mm diameter aperture (collimator C1) separates the hexapole chamber from the chopper chamber. The hexapole region houses an electrostatic hexapole. The hexapole assembly consists of six highly polished cylindrical stainless steel rods, each 12.68 ± 0.03 mm in diameter and 193.0 ± 0.03 cm long with hemispherical ends. Mounting yokes hold the rods in a hexagonal array with an internal radius, $r_0 = 9.6 \pm 0.1$ mm (distance from center axis to pole face; the error indicates variations in r_0 along the entire length of the hexapole).[25] Alternating rods are biased at positive and negative potentials (up to $V_0 = \pm 30$ kV) with respect to the grounded chamber using programmable power supplies. A 2.54 mm diameter electrically grounded beam-stop, located approximately halfway along the machine length and in the center of the hexapole, is used to intercept nonfocusing beam components (e.g. atoms, nonpolar molecules) as well as focused radicals with trajectories that have a node at the beam-stop position. The beam-stop position can be manipulated *in situ* to optimize its interception of the direct beam.

A 1.5 mm diameter aperture (collimator C2) separates the detector chamber from the hexapole chamber. The detector chamber houses a custom-made electron impact quadrupole mass spectrometer (EI-QMS) that measures the number densities of different components of the molecular beam. The axial ionizer is followed by an electrostatic quadrupole[26] that turns the ion beam by 90° with respect to the molecular beam axis. This enables the un-ionized portion of the molecular beam to pass through the ionizer unobstructed. The ion beam is focused into a radio frequency (rf) quadrupole mass filter (rod diameter = 19 mm; length = 219 mm) powered by an rf power supply. The ionizer controller was custom-built and typically operates the ionizer with an electron energy of 70 eV and emission current of 2 mA. The analog ion current transmitted by the mass filter is amplified by a discrete dynode chain multiplier and current preamplifier. The output of the preamplifier is directed to either a lock-in amplifier for phase-sensitive detection or to a digital oscilloscope for time-of-flight measurements. The lock-in amplifier output is digitized by a PC computer-based data acquisition board. The data acquisition board is also used to program the mass setting on the EI-QMS detector and the hexapole rod voltage.

The significant experimental results reported in this paper correspond to what is termed focusing spectra (see, for example, Figure 4). These are measured by monitoring the flux density of hydroxyl radicals transmitted through the hexapole exit collimator (C2) as a function of the hexapole voltage, V_0. The flux density is measured with the EI-QMS detector in the configuration employing the lock-in amplifier and phase-

sensitive detection. The following provides details on calibrating the lock-in amplifier output to provide estimates of absolute flux densities.

The absolute rare gas atom beam flux is measured with an ion gauge accumulation type detector. The flux, F (in particles s^{-1}), is given by:[27]

$$F = \Delta PC/kT \tag{1}$$

where ΔP is the pressure rise measured in the ion gauge due to the beam, C is the conductance of the beam gas through the 3.4 mm diameter aperture (collimator C4) to the ion gauge, k is Boltzmann's constant, and T is the temperature of the gauge. An intense Ar atom beam produced a $\Delta P = 1 \times 10^{-7}$ Torr that corresponds to a beam flux of 5.9×10^{12} Ar atoms s^{-1}. We calibrate the EI-QMS detector against the ion gauge flux detector. The absolute beam flux, F, is converted to number density (n_i) in the EI-QMS detector by dividing F by the stream velocity, v_s (see below), and the area of the collimator that limits the beam diameter, in this case C2. At a given mass, j, the electron current from the EI-QMS multiplier, I_j, is given by

$$I_J = \gamma \sum_i \sigma_{ij} n_i \tag{2}$$

where γ is a calibration constant, σ_{ij} is the partial ionization cross section for making an ion of mass j from neutral i, and n_i is the number density of neutral i. In a series of calibration experiments using fluorocarbon compounds with complex cracking patterns, we have determined that γ is nearly independent of mass in our mass spectrometer. For an Ar atom beam, we measured $n_{Ar} = 4.3 \times 10^9$ Ar atoms cm^{-3} (for the OH seeded in Ar data, see section 4) using the ion gauge flux detector with $\sigma_{Ar,40} = 2.57$ Å^2.[28] This determined the calibration constant γ. We can determine the number density of any component in the beam provided we know the corresponding partial ionization cross-section. Becker and co-workers have recently measured the absolute partial ionization cross-section for the hydroxyl radical at an electron energy of 70 eV ($\sigma_{OH,17} = \sigma_{OD,18} = 1.75$ Å^2).[29,30] The absolute hydroxyl radical flux densities reported in this paper were determined by applying the above methodology to determine the number densities and then multiplying the number densities by the stream velocity (i.e., $J = n_i v_s$). In the experiments reported herein, achieving the maximum possible hydroxyl radical beam intensity was not always our paramount objective. Conditions were optimized for rotational state resolution, as well, particularly for the OD spectra.

The distribution of velocities of particles in the beam is determined using standard time-of-flight techniques.[31] The velocity distributions are deconvolved from measured time-of-flight distributions using an instrument response function measured by applying a step potential to one of the ion lenses in the EI-QMS ionizer. Velocity distributions are characterized by fitting them to the following standard form:[32]

$$n(v) \propto v^2 \exp[-(v - v_s)^2/\alpha_s^2] \tag{3}$$

where $n(v)$ is the number density speed distribution, v_s is the stream velocity, and $\alpha_s = (2kT_s/m)^{1/2}$ with T_s being the translational temperature, m the mass-weighted mass of the gas mixture, and k Boltzmann's constant.

3. Focusing Theory and Molecular Trajectory Simulations

Calculating the trajectories of polar molecules traversing an electrostatic hexapole requires a detailed understanding of the radial force exerted on the molecule by the inhomogeneous electric field of the hexapole. Given an accurate theoretical expression for the radial force, F_r, one can easily integrate Newton's equations of motion, either numerically or analytically, and determine the classical molecular trajectory through the field. The radial force is given by

$$F_r = -\frac{\partial W_\epsilon}{\partial r} = -\frac{\partial W_\epsilon}{\partial \epsilon}\frac{\partial \epsilon}{\partial r} = \mu_{eff}\frac{\partial \epsilon}{\partial r} \tag{4}$$

where W_ϵ is the molecular energy which will depend on the electric field strength ϵ, and $\mu_{eff} \equiv -\partial W_\epsilon/\partial \epsilon$ is the effective dipole moment. The radial field gradient is assumed to be that of an ideal hexapole, that is:[33]

$$\partial \epsilon/\partial r = (6V_0/r_0^3)r \tag{5}$$

where V_0 is the hexapole voltage, r_0 is the radial distance from the central axis of the hexapole to a hexapole face, and r is the radial coordinate with the constraint $r \le r_0$. The task is to determine the gradient in the field-dependent rotational energy levels with respect to the electric field, $\partial W_\epsilon/\partial \epsilon$.

Past trajectory simulations of focusing spectra for symmetric top molecules have relied on first-order[34,35] and, more recently, second-order[36,37] perturbation theory. Similar first-order treatments have been used to simulate focusing spectra of the linear species N_2O vibrationally excited in the ν_2 bending mode[38] as well as diatomic molecules in $^2\Pi_\Omega$ electronic states. The latter case of the $^2\Pi$ diatomics is directly relevant to OH/OD focusing. Kuwata and Kasai assumed a pseudo-symmetric top approximation to simulate focusing spectra for CH and SH radicals.[39] This approximation ignores effects due to Λ-doubling, spin−orbit coupling, and hyperfine interactions. We have found that the first two effects significantly influence the focusing behavior of CF,[23] OH, and OD. On the basis of the magnitudes of their Λ-doubling constants and spin−orbit coupling constants, we would expect these effects to be manifested in the focusing behavior of CH and, to a lesser extent, SH, as well. See Table 2 for a comparison of molecular constants listed for OH, OD, NO, CH, SH, and CF. We incorporate a more rigorous treatment of the Stark effect in our focusing simulations that includes Λ-doubling and spin−orbit coupling effects. Results of trajectory simulations for CF radicals using these methods have been reported.[23]

We approach the task of calculating the Stark shifts in the rotational energy levels by constructing an effective Hamiltonian for the system. It is straightforward to incorporate Λ-doubling and spin−orbit coupling effects into the treatment of the Stark effect by incorporating these terms into the unperturbed rotational Hamiltonian, H_0:[53]

$$H_0 = B(r)(\mathbf{J} - \mathbf{L} - \mathbf{S})^2 + A(r)\mathbf{L}\cdot\mathbf{S} \tag{6}$$

TABLE 2: Molecular Constants of Selected $^2\Pi_\Omega$ Radicals

molecule	A_0 (cm^{-1})	B_0 (cm^{-1})	μ (D)	ν_Λ (MHz)	$\|J\ \Omega\rangle$
OH	−139.2[a]	18.5[a]	1.667[b]	1667[a]	$\|^3/_2\ ^3/_2\rangle$
OH	−139.2[a]	18.5[a]	1.667[b]	6034[a]	$\|^5/_2\ ^3/_2\rangle$
OD	−139.2[f]	9.9[c]	1.653[b]	310[d]	$\|^3/_2\ ^3/_2\rangle$
OD	−139.2[f]	9.9[c]	1.653[b]	1190[d]	$\|^5/_2\ ^3/_2\rangle$
NO	123.2[e]	1.7[f]	0.159[g]	356[h]	$\|^1/_2\ ^1/_2\rangle$
CF	77.11[f]	1.4[f]	0.645[m]	257[m]	$\|^1/_2\ ^1/_2\rangle$
CH	28.1[i]	14.2[i]	1.46[g]	3349[j]	$\|^1/_2\ ^1/_2\rangle$
SH	−376.8[k]	9.5[k]	0.758[g]	111[l]	$\|^3/_2\ ^3/_2\rangle$

[a] Reference 40. [b] Reference 41. [c] Reference 42. [d] Reference 43. [e] Reference 44. [f] Reference 45. [g] Reference 46. [h] Reference 47. [i] Reference 48. [j] Reference 49. [k] Reference 50. [l] Reference 51. [m] Reference 52.

where **J**, **L**, and **S** are angular momentum operators corresponding the total angular momentum, the total electronic orbital angular momentum, and the total electronic spin angular momentum, respectively. The first term in eq 6 corresponds to the nuclear end-over-end rotational Hamiltonian and the second term to a phenomenological spin−orbit Hamiltonian. Our basis functions are $|n^2\Pi_\Omega v JM\rangle$ which may be separated into electronic orbital, electronic spin, rotational, and vibrational components $|n\Lambda\rangle|S\Sigma\rangle|J\Omega M\rangle|v\rangle$. Parity-labeled eigenfunctions $|n^2\Pi_\Omega v JMp^\pm\rangle$ may be formed from symmetric and antisymmetric combinations of the basis functions (see ref 53). The $p^\pm$ parity is but one type of parity, total parity. The two other major parity labeling schemes are rotationless (*e*/*f*) and (A′/A″) parity. The A′/A″[54] labeling corresponds to the electron cloud orientation in the $^2\Pi$ molecule. For the $^2\Pi_{3/2}$ rotational manifold of OH and OD, the *f*-states are labeled A″, and *e*-states are A′ (see previous reference).

By expanding H_0 and excluding contributions from $B(\mathbf{L}_x^2 + \mathbf{L}_y^2)$, one obtains an effective Hamiltonian $\mathbf{H}_{\text{eff}} = \mathbf{H}_{\text{rot.}}^{(v)} + \mathbf{H}_{\text{SO}}^{(v)} + \mathbf{H}_{\Lambda}^{(v)}$. $\mathbf{H}_{\text{eff}}$ is composed of vibrational level-dependent (v) rotational ($\mathbf{H}_{\text{rot.}}$), spin−orbit ($\mathbf{H}_{\text{SO}}$), and Λ-doubling ($\mathbf{H}_\Lambda$) contributions. The energy levels of $\mathbf{H}_{\text{eff}}$ are given as:[53]

$$W^0(|n^2\Pi_{3/2} v JM\text{A}''/\text{A}'\rangle) = B_v\left[\left(J-\frac{1}{2}\right)\left(J+\frac{3}{2}\right) - \frac{1}{2}X\right] \pm \frac{h\nu}{2} \quad (7)$$

with the A″ states associated with the upper sign on the right of eq 7, the A′ states associated with the lower sign, and

$$W^0(|n^2\Pi_{1/2} v JM\text{A}'/\text{A}''\rangle) = B_v\left[\left(J-\frac{1}{2}\right)\left(J+\frac{3}{2}\right) + \frac{1}{2}X\right] \pm \frac{h\nu_\Lambda}{2} \quad (8)$$

with the A′ states associated with the upper sign on the right of eq 8 and the A″ states associated with the lower sign. The other parameters in eqs 7 and 8 are defined below:

$$X = \left[4\left(J+\frac{1}{2}\right)^2 + Y(Y-4)\right]^{1/2} \quad (9)$$

where $Y = A_v/B_v$ (A_v and B_v are the vth-level vibrational spin−orbit and rotational constants, respectively), J is the rotational quantum number, h is Planck's constant, and ν_Λ is the Λ-doubling frequency. The intermediate Hund's case a/b wave functions are given by

$$|\Psi(F_1)\rangle = a_J|^2\Pi_{1/2} JM\rangle + b_J|^2\Pi_{3/2} JM\rangle$$

$$|\Psi(F_2)\rangle = -b_J|^2\Pi_{1/2} JM\rangle + a_J|^2\Pi_{3/2} JM\rangle \quad (10)$$

where

$$a_J = \left[\frac{X+(Y-2)}{2X}\right]^{1/2}$$

$$b_J = \left[\frac{X-(Y-2)}{2X}\right]^{1/2} \quad (11)$$

and F_1 corresponds to energy levels calculated for states with predominately $|\Omega = {}^3/_2|$ character and F_2 to levels calculated with predominately $|\Omega = {}^1/_2|$ character. All wave functions are linear combinations of Hund's case a basis functions and will be denoted with the $|J\Omega M\text{A}'\rangle$ or $|J\Omega M\text{A}''\rangle$ representation for further considerations; however, we will label the corresponding rotational eigenstates (in $v = 0$ of $X^2\Pi_\Omega$) with the $|J \pm\Omega \pm M\rangle$ or $|J \pm\Omega \mp M\rangle$ designations.

An electric field will modify the rotational energies by introducing an additional term into the Hamiltonian, namely,

$$\mathbf{H}_\epsilon = -\sum_{Fg} \mu_g \epsilon \Phi_{Fg} \quad (12)$$

where F represents the laboratory frame coordinates X, Y, or Z and g represents the molecule-fixed frame coordinates x, y, or z. The permanent electric dipole moment μ defines the molecular z axis. In OH(OD), μ is directed along the internuclear axis with no orthogonal components; the x and y magnitudes of the dipole moment are zero. Also, we just consider the radial, homogeneous component of the electric hexapole field and choose this as the quantization axis Z with no other electric fields along X or Y. Under these conditions, eq 12 simplifies to the following:

$$\mathbf{H}_\epsilon = -\mu_\epsilon \Phi_{Zz} \quad (13)$$

The Φ_{Zz} are the direction cosines.[55] $\mathbf{H}_\epsilon$ does not connect different Ω or M_J (i.e., $\Delta\Omega = \Delta M_J = 0$) but does connect states of different parity (i.e., A′ and A″ states with the same Ω and M_J), and the interaction is simply $\langle J\Omega M\text{A}'|\Phi_{Zz}|J\Omega M\text{A}''\rangle = \langle J\Omega M\text{A}''|\Phi_{Zz}|J\Omega M\text{A}'\rangle = \langle\Phi_{Zz}\rangle = \Omega M/[J(J+1)]$. The 2 × 2 secular determinant is

$$\begin{array}{lcc} & |J\Omega M\text{A}''\rangle & |J\Omega M\text{A}'\rangle \\ \langle J\Omega M\text{A}''| & W^\circ_{J\Omega M\text{A}''} - W_\epsilon & -\mu\epsilon\dfrac{\Omega M}{J(J+1)} \\ \langle J\Omega M\text{A}'| & -\mu\epsilon\dfrac{\Omega M}{J(J+1)} & W^\circ_{J\Omega M\text{A}'} - W_\epsilon \end{array} \quad (14)$$

The secular determinant has up to second-order corrections for the nondegenerate states. Solving this 2 × 2 yields the eigenvalues for the Stark energies.

$$W_\epsilon = \frac{W^\circ_{J\Omega M\text{A}''} + W^\circ_{J\Omega M\text{A}'}}{2} \pm \left[\frac{(W^\circ_{J\Omega M\text{A}''} - W^\circ_{J\Omega M\text{A}'})^2}{4} + \mu^2\epsilon^2\left(\frac{\Omega M}{J(J+1)}\right)^2\right]^{1/2} \quad (15)$$

This leads to the proper derivative for the radially-dependent force:

$$F_r = -\frac{\partial W_\epsilon}{\partial r} = -\frac{\partial W_\epsilon}{\partial \epsilon}\frac{\partial \epsilon}{\partial r}$$

$$= \mp\left[\frac{(W^\circ_{J\Omega M\text{A}''} - W^\circ_{J\Omega M\text{A}'})^2}{4} + \mu^2\epsilon^2\left(\frac{\Omega M}{J(J+1)}\right)^2\right]^{-1/2} \mu^2\left(\frac{\Omega M}{J(J+1)}\right)^2 \epsilon\frac{\partial \epsilon}{\partial r} \quad (16)$$

The Stark energy calculated using eq 15 is shown in Figure 2 for several low-lying rotational states of OH and OD. Notice the Stark energy curves are largely linear for the characteristic field strengths of our instrument (i.e., $\mp \leq 100$ kV cm^{-1}). The spin−orbit interaction affects these Stark energies by changing the slopes of these curves slightly. As an example, the $|{}^5/_2\ \pm{}^3/_2\ \mp{}^5/_2\rangle$ rotational state of Figure 2 has a slope that is 95% of the slope for the same state excluding spin−orbit mixing. One would expect OH and OD to have a dominant first-order Stark effect and focus much like polar symmetric top molecules, as well they do, but early in the energy curves there is a slight curvature due to the Λ-doubling interaction. The curvature is better seen in a derivative plot of the Stark energy, $-\partial W_\epsilon/\partial\epsilon$

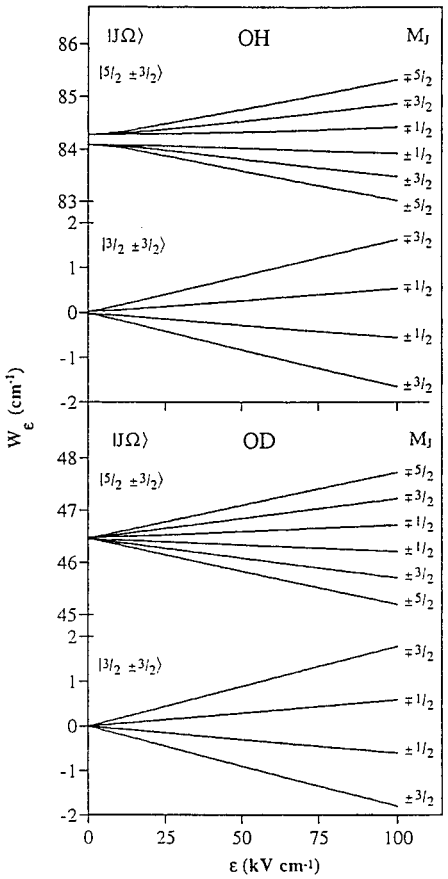

Figure 2. Stark energy diagrams for the two lowest $|J\Omega\rangle$ rotational levels of OH and OD, the $|^3/_2 \pm ^3/_2\rangle$ and $|^5/_2 \pm ^3/_2\rangle$ rotational states. The nonlinearity in the energy levels, particularly in the $|^5/_2 \pm ^3/_2\rangle$ states of OH, is caused by Λ-doubling and leads to the deviation in the focusing behavior for these two molecules. The field strengths ϵ shown are characteristic of our hexapole instrument.

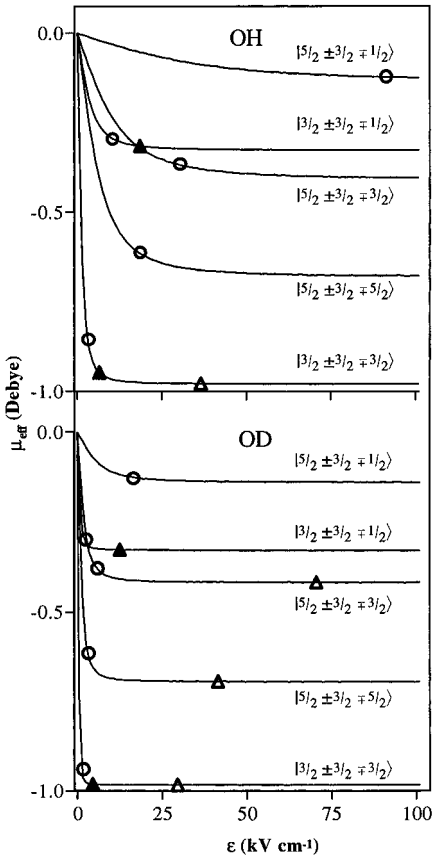

Figure 3. Effective dipole moment plots for the spin−orbit mixed, focused states of OH and OD. The circles denote 90% of the high-field saturation limit for the effective dipole of the spin−orbit mixed rotational states. The triangles indicate the maximum radial field strengths at $r = r_0$ at values of V_0 corresponding to resonance. Closed triangles represent Ar seeded beams, while open triangles represent He seeded beams. For the $|^3/_2 \pm ^3/_2 \mp ^3/_2\rangle$ rotational state in the high-field limit, $\mu_{eff} \approx 0.97$ D for OH and $\mu_{eff} \approx 0.98$ D for OD.

versus ϵ (from eq 4, $\mu_{eff} = -\partial W_\epsilon/\partial\epsilon$), as shown in Figure 3. Recall that μ_{eff} is proportional to the radial force felt by the molecule in the hexapole field (eq 4). One sees in Figure 3 that the magnitude of the radial force increases from zero to a limiting, high-field value, namely, $\mu_{eff}^{lim} = \mu\Omega M/J(J+1)$, where Ω is weighted by spin−orbit mixing. The field necessary to produce this limit depends on the rotational state. The open circles shown in Figure 3 are located at points where μ_{eff} is at 90% of the high-field limit, and the triangles indicate field strengths near the poles at $r = r_0$ for values of V_0 corresponding to the resonance features in the measured focusing spectra discussed below. The effect caused by the Λ-doubling interaction can significantly increase the resonance voltage for state selection at low field strengths.

The treatment used here for calculating the energies of the Λ-doubled levels (eqs 7 and 8 for the field-free case) is analogous to that developed for nearly degenerate energy levels of asymmetric rotors,[56,57] *l*-doubling in linear polyatomic molecules owing to excited bending modes,[56,57] inversion levels of symmetric tops,[56] and hindered rotations (as in H_3C-CH_3).[56,57] The radial force equation developed in eq 16 can easily be applied in trajectory simulations of the focusing behavior of these molecules as well. Experimental focusing spectra for many of these types of molecules have been reported: asymmetric tops, SO_2,[58] CH_2Cl_2,[58,59] CH_3NO_2, and CD_3OD;[59] excited ν_2-bending states in linear triatomics, N_2O,[38] OCS,[59,60] and BrCN;[59] and inverting molecules, NH_3[39,59,60] and ND_3.[60]

With the force equation in hand, one can now calculate trajectories through the hexapole field using Newton's laws of motion and simulate focusing spectra. Our treatment does ignore two subtleties that in some cases lead to effects as dramatic as the Λ-doubling effect observed in OH/OD focusing, namely, hyperfine and rotational state interactions. The first excited rotational state of OH is some 88 cm^{-1} above the ground and 46 cm^{-1} for OD. Consequently, the mixing of states with different *J* quantum numbers by the electric field is negligible for these systems. We could easily incorporate *J*-mixing effects by expanding the 2×2 secular determinant shown in eq 14 to include states of different *J*. The hyperfine problem is unimportant in OH since there are no nuclear spins ≥ 1;[61] however, hyperfine may occur in OD (deuterium nuclear spin $I = 1$). Hyperfine effects can be incorporated by including an additional hyperfine term in the effective Hamiltonian, $\mathbf{H}_{eff}$. In practice, this is complicated since the electric field decouples the nuclear spin angular momentum (momenta) from the other angular momenta in the molecule. We have neglected hyperfine effects in our treatment of OD.

In our trajectory program, we assume straight line trajectories in all field-free regions and use an ideal hexapole potential in the field regions. We perform a numerical integration of Newton's third law force equation to calculate trajectories. The initial conditions used are rotational state, radial position, radial and axial velocities, hexapole voltage, and axial position step size. The trajectory of a single rotational state is initiated at the entry of the hexapole. The ultimate radial position at the end of the hexapole is determined after traversing the hexapole length, and a straight line trajectory is taken from that position

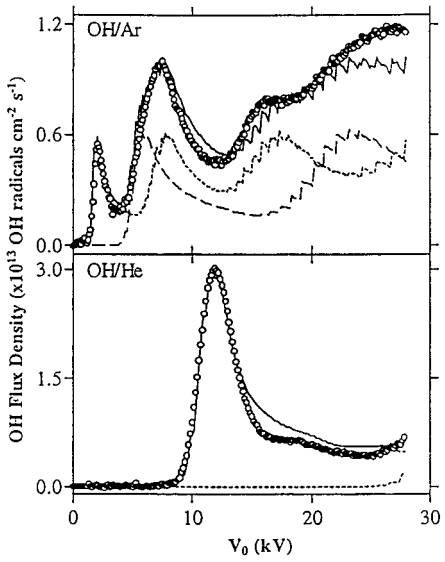

Figure 4. Focusing spectra of OH seeded in Ar (top panel) and OH seeded in He (bottom panel). For both panels, the open circles are experimental data, while the dotted and dashed lines are trajectory simulations for the $|^3/_2\ \pm^3/_2\ \mp^3/_2\rangle$ and the $|^3/_2\ \pm^3/_2\ \mp^1/_2\rangle$ rotational states, respectively. The solid line is the sum of simulations for both states.

until the final collimator C2 is reached. The radial position must be within the radius of C2, or the trajectory is terminated. If within C2, the trajectory continues with a constant slope until the detector aperture is reached (corresponding to our EI-QMS collimator C3). If within C3, the trajectory is counted as successful, and a new trajectory calculation begins.

We approximate our beam source as a point and obtain the starting position at the hexapole with the constraint that the trajectory from the source must be within the radii of the skimmer and C1. Furthermore, the limiting angle of entry into the hexapole is defined by the angle between the hexapole axis and a ray extending from the point source to the edge of C1. With this maximum angle of deflection given, we start at $0 \leq r_{\text{initial}} \leq 1.82$ mm for the initial radial position at the hexapole entrance with $\Delta r_{\text{initial}} = 0.085$ mm. The allowed slopes (and thus radial velocities) are therefore defined by this value of r_{initial}. The velocity distribution used is that of eq 3 with T_s, v_s, and Δv (velocity step size) the input parameters. The step size of the axial length of the hexapole and hexapole voltage are $\Delta\text{hex} = 1$ mm and $\Delta V_0 = 0.1$ kV. The ultimate output of the program is an array of numbers composed of the voltage of the hexapole and the corresponding enhancement. The calculations of enhancements are algorithms developed by Chakravorty et al.[34] and previously used by Choi *et al.*[35,62] We scaled the output to our experimental data while conserving relative state enhancements.

4. Results

Focusing spectra measured for OH seeded in Ar (upper panel) and He (lower panel) are shown by the open circles in Figure 4. The Ar seeded beam was characterized by a stream velocity, $v_s = 702$ m s^{-1}, and translational temperature, $T_s = 8$ K. The backing pressure was 1700 Torr. The discharge source conditions used were +3.3 kV bias potential and 0.7 mA discharge current. For the He seeded beam v_s and T_s were 1850 m s^{-1} and 3 K, respectively. The discharge was operated at 4 kV and 0.8 mA at a backing pressure of 1700 Torr. Also shown in Figure 4 are corresponding trajectory simulations. The broken lines correspond to simulated spectra for individual rotational states, and the solid lines correspond to the sum of all states contributing to the total hydroxyl radical flux.

Under the conditions reported here for OH, only two states were appreciably populated, the energetically lowest $|^3/_2\ \pm^3/_2\ \mp^3/_2\rangle$ and $|^3/_2\ \pm^3/_2\ \mp^1/_2\rangle$ rotational states. Assuming a thermal distribution from the source, these two states should be equally populated. Such was assumed for the simulations. If we assume that the rotational temperature is comparable to the translational temperature, then we would expect a thermal population ratio for states in the $|^5/_2\ \pm^3/_2\ \mp M_J\rangle$ manifold to the $|^3/_2\ \pm^3/_2\ \mp M_J\rangle$ states of less than 10^{-6}. However, nonthermal distributions are suggested by population distributions seen in the OD focusing spectra discussed below. On the basis of our ability to resolve and simulate rotational features in Figure 4, we estimate the populations of the $|^5/_2\ \pm^3/_2\ \mp M_J\rangle$ states to be less than 4% of the $|^3/_2\ \pm^3/_2\ \mp M_J\rangle$ states.

Several observations from Figure 4 are worth noting. The general structure of the focusing spectra can easily be understood from the nearly linear dependence of the Stark energy on field strength (see Figure 2). Molecules exhibiting a linear, first-order Stark effect execute purely sinusoidal radial trajectories in a hexapole field.[33] Therefore, a given rotational state will first appear after undergoing a half-wave trajectory ($n \equiv$ the number of half-wave sine loops = 1) and then will reappear from full-wave ($n = 2$), three-halves-wave ($n = 3$), etc., trajectories. Moreover, the solution to the first-order force equation shows that the resonance voltage is proportional to n^2.[33] We see just this approximate behavior in the Ar seeded spectrum in Figure 4: the $|^3/_2\ \pm^3/_2\ \mp^3/_2\rangle$ states focused at 2, 8, and 16 kV corresponding to $n = 1$, 2, and 3, respectively, while the $|^3/_2\ \pm^3/_2\ \mp^1/_2\rangle$ states focused at 6 and 23 kV corresponding to $n = 1$ and 2, respectively. Enhancement in the focused OH beam intensity over the direct, unfocused OH beam intensity was difficult to quantify because the direct beam contained both OH and H_2O, and each contributed to the EI-QMS signal at $m/e = 17$. Enhancements in the total $m/e = 17$ signal for the $n = 1$ trajectory of the $|^3/_2\ \pm^3/_2\ \mp^3/_2\rangle$ state were typically ~13. This gives a lower bound on the focusing enhancement for the OH in the beam.

The agreement between the simulated and experimental focusing spectra is generally good,[25] particularly at low hexapole voltages. Achieving such good agreement *requires* the incorporation of the Λ-doubling effect into the trajectory calculations. The calculated and measured peak positions for the $n = 1$ trajectory of the $|^3/_2\ \pm^3/_2\ \mp^3/_2\rangle$ state occur at $V_0 = 2.05$ and 12.0 kV for OH seeded in Ar and He, respectively (see Figure 4). The same peak positions calculated using the psuedo-symmetric top approximation that ignores the Λ-doubling interactions would occur at $V_0 = 1.69$ and 10.6 kV for Ar and He, respectively. This difference highlights the impact Λ-doubling has on peak position, particularly at low field strengths. The effect is even more dramatic for other states (see Figures 2 and 3). The apparent "noise" in the simulated spectra at high voltages is an artifact of the simulations due to numerical integration using a finite step size.

The rotational state resolution is good, and the absolute beam flux densities are high. These attributes are due to the dramatic collisional cooling achieved in the supersonic corona discharge source. As mentioned previously, very few rotational states are populated, and the velocity distributions are narrow. Ideally, we would like to isolate specific rotational states for detailed molecular dynamics scattering experiments. One sees from Figure 4 that isolation of the $|^3/_2\ \pm^3/_2\ \mp^3/_2\rangle$ state with better than 99% purity was easily achieved by fixing the hexapole voltage to the peak position of the $n = 1$ trajectory (e.g., $V_0 = 2.05$ for OH in Ar). However, the $n = 1$ trajectory of the $|^3/_2\ \pm^3/_2\ \mp^1/_2\rangle$ state was "contaminated" by the $n = 2$ trajectory

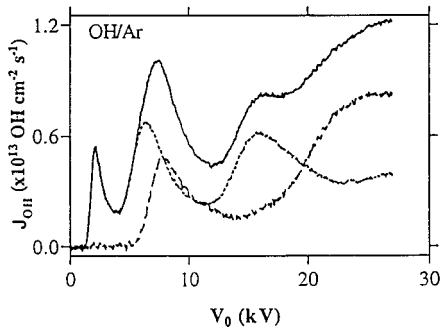

Figure 5. Focusing spectra taken with and without the beam stop intercepting the direct, unfocused beam and even *n* trajectories (see text for details). The solid line is data for OH/Ar without the beam stop imposed in the beam line. The dotted line is an experimantal focusing spectrum for OH/Ar with the beam stop in the beam line. The dashed curve is the difference of the beamstop and no beam stop data sets and indicates the parts of the focusing spectrum from even *n* trajectories that are eliminated from the beam with the beam stop in place.

of the $|^3/_2\ \pm^3/_2\ \mp^3/_2\rangle$ state. One can discriminate against the latter by inserting a beam stop at the center of the hexapole where n = even-numbered trajectories have a node and are blocked. Figure 5 shows the effect a beam stop had on the focusing spectrum of OH/Ar. The solid curve was measured without the beam stop (same data as in Figure 4), the dotted curved was measured with the beam stop, and the dashed curve is the difference. By comparing the difference curve in Figure 5 with the simulated spectrum for the $|^3/_2\ \pm^3/_2\ \mp^3/_2\rangle$ state shown in the upper panel of Figure 4, one can immediately see that the $n = 2$ trajectory of the $|^3/_2\ \pm^3/_2\ \mp^3/_2\rangle$ state was largely eliminated by the beam stop, enabling us to better isolate the $|^3/_2\ \pm^3/_2\ \mp^1/_2\rangle$ state. We estimate that the rotational state composition using the beam stop was 81% $|^3/_2\ \pm^3/_2\ \mp^1/_2\rangle$ and 19% $|^3/_2\ \pm^3/_2\ \mp^3/_2\rangle$ at $V_0 = 6.4$ kV. As will be discussed below, these two states have dramatically different orientational probability distributions. Our ability to isolate them enhances our capability of exploring steric effects in chemical reactivity.

The focusing spectrum of OD seeded Ar (upper panel) and He (lower panel) were also measured and are shown in Figure 6 along with the corresponding trajectory simulations. The beam characteristics for the Ar seeded beam were similar to those used for OH in Ar. The Ar seeded beam was characterized by a stream velocity, $v_s = 650$ m s^{-1}, and translational temperature, $T_s = 8$ K. The backing pressure was 1650 Torr. The discharge source conditions used were +3.8 kV bias potential and 0.8 mA discharge current. The upper panel of Figure 6 shows that for OD seeded in Ar we were able to clearly resolve the $n = 1$ trajectory of the $|^3/_2\ \pm^3/_2\ \mp^1/_2\rangle$ at $V_0 = 4.3$ kV from the $n = 2$ trajectory of the $|^3/_2\ \pm^3/_2\ \mp^3/_2\rangle$ state at $V_0 = 5.7$ kV. This observation once again highlights the Λ-doubling effect. The Λ-doubling constant is five times smaller for OD than OH (see Figures 2 and 3). Consequently, the Stark energy saturates to the high-field limit at lower field strengths for OD, resulting in more narrow focusing peaks. Because the rotational state energy level spacing for OD is only half that of OH, we found that expansions of OD seeded in He populated states in the $|^5/_2\ \pm^3/_2\ \mp M_J\rangle$ rotational manifold as well as the $|^3/_2\ \pm^3/_2\ \mp M_J\rangle$ manifold. The OD/He beam was characterized by $v_s = 1710$ m s^{-1} and $T_s = 6$ K with the discharge operated at 0.15 mA and 1600 Torr backing pressure. The lower panel of Figure 6 shows evidence for focusing two new states, the $|^5/_2\ \pm^3/_2\ \mp^5/_2\rangle$ state at 13.5 kV and the $|^5/_2\ \pm^3/_2\ \mp^3/_2\rangle$ state at 23 kV. The simulated focusing spectra for these two states have been offset for the sake of clarity. From the apparent population ratio between the $|^3/_2\ \pm^3/_2\ \mp M_J\rangle$ states and the $|^5/_2\ \pm^3/_2\ \mp M_J\rangle$

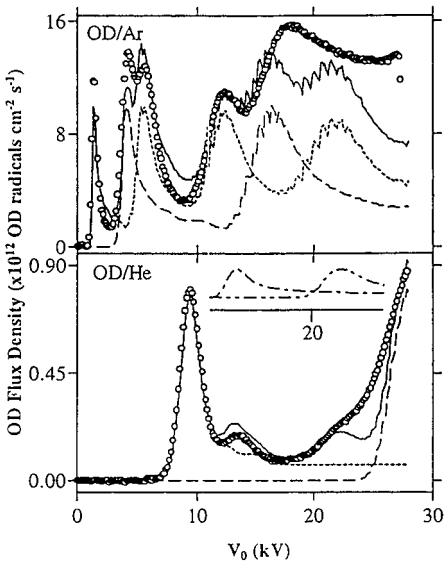

Figure 6. Focusing spectra for OD seeded in Ar (top panel) and seeded in He (bottom panel). For both panels, the open circles are experimental data, while the dotted and dashed lines are trajectory simulations for the $|^3/_2\ \pm^3/_2\ \mp^3/_2\rangle$ and the $|^3/_2\ \pm^3/_2\ \mp^1/_2\rangle$ rotational states, respectively. For the lower panel, the inset is a truncation of the simulated focusing spectra for the $|^5/_2\ \pm^3/_2\ \mp^5/_2\rangle$ (dotted−dashed line) and the $|^5/_2\ \pm^3/_2\ \mp^3/_2\rangle$ (dotted−dotted−dashed line) rotational states. The solid line is the sum of all simulations.

states, we can estimate a rotational temperature of 130 K, a value substantially greater than the translational temperature. Typically, the rotational and translational temperatures are comparable in supersonic expansions. This suggests we do not have a Boltzmann rotational state distribution, an observation seen previously by ter Muelen and co-workers.[63]

Finally, a few observations on the operation of the corona discharge source and its effects on focusing are appropriate. More aggressive discharge conditions reduce the rotational state resolution in the focusing spectra. This effect is due to an increased velocity dispersion. However, under these conditions higher flux densities of OH (OD) radicals were observed. As one increases the discharge current, the source also becomes less stable, and over extended periods (days) at ≫1 mA discharge current, the nozzle orifice becomes larger and irregularly shaped. These tradeoffs are demonstrated in Figure 6, where the low beam intensities seen in the OD/He spectrum reflect our effort to resolve the additional rotational states present by working at a relatively low discharge current of 0.15 mA.

5. Discussion

Several groups have used electric field deflection methods to focus and state-select molecules for studies of stereodynamical effects in molecular scattering.[39,64−67] The utility of the deflection method derives from rotational state-selection and the highly anisotropic spatial distributions of molecules populating specific rotational states. The orientational behavior of symmetric top molecules has been described by Choi and Bernstein.[68] For the diatomic case, Stolte has analyzed the orientational behavior of NO in several of its lowest rotational states.[69] We extend this work to include OH and OD by making minor adjustments to account for the spin−orbit mixing pertinent to the hydroxyl radical.

We describe the probability distribution function (pdf) for the orientation of the molecular axis relative to the local electric field vector with a Legendre polynomial expansion:[68]

TABLE 3: Orientational Probability Distribution Function Coefficients[a]

molecule	state	a_J2	b_J2	C_0	C_1	C_2	C_3	C_4	C_5
OH	$\|^3/_2 \pm^3/_2 \mp^3/_2\rangle$	0.97	0.03	0.500	0.882	0.470	0.088	0.000	0.000
OH	$\|^3/_2 \pm^3/_2 \mp^1/_2\rangle$	0.97	0.03	0.500	0.294	−0.470	−0.264	0.000	0.000
OH	$\|^5/_2 \pm^3/_2 \mp^5/_2\rangle$	0.93	0.07	0.500	0.613	−0.216	−0.566	−0.284	−0.047
OH	$\|^5/_2 \pm^3/_2 \mp^3/_2\rangle$	0.93	0.07	0.500	0.368	0.043	0.792	0.851	0.235
OH	$\|^5/_2 \pm^3/_2 \mp^1/_2\rangle$	0.93	0.07	0.500	0.122	0.173	0.453	−0.568	−0.470
OD	$\|^3/_2 \pm^3/_2 \mp^3/_2\rangle$	0.99	0.01	0.500	0.893	0.489	0.096	0.000	0.000
OD	$\|^3/_2 \pm^3/_2 \mp^1/_2\rangle$	0.99	0.01	0.500	0.298	−0.489	−0.286	0.000	0.000
OD	$\|^5/_2 \pm^3/_2 \mp^5/_2\rangle$	0.97	0.03	0.500	0.631	−0.194	−0.576	−0.306	−0.054
OD	$\|^5/_2 \pm^3/_2 \mp^3/_2\rangle$	0.97	0.03	0.500	0.378	0.039	0.807	0.919	0.272
OD	$\|^5/_2 \pm^3/_2 \mp^1/_2\rangle$	0.97	0.03	0.500	0.126	0.155	0.461	−0.612	−0.545
case a	$\|^3/_2 \pm^3/_2 \mp^3/_2\rangle$	1.00	0.00	0.500	0.900	0.500	0.100	0.000	0.000
case a	$\|^3/_2 \pm^3/_2 \mp^1/_2\rangle$	1.00	0.00	0.500	0.300	−0.500	−0.300	0.000	0.000
case a	$\|^5/_2 \pm^3/_2 \mp^5/_2\rangle$	1.00	0.00	0.500	0.643	−0.178	−0.583	−0.321	−0.060
case a	$\|^5/_2 \pm^3/_2 \mp^3/_2\rangle$	1.00	0.00	0.500	0.386	0.036	0.817	0.964	0.298
case a	$\|^5/_2 \pm^3/_2 \mp^1/_2\rangle$	1.00	0.00	0.500	0.128	0.143	0.467	−0.643	−0.595

[a] Expansion coeeficients for spin−orbit mixed orientational probablility distribution functions for OH and OD in particular rotational states $|J\Omega M\rangle$. The bottom five entries are non-spin−orbit-mixed, Hund's case a orientational probabilities in the high-field limit. Note: each C_n entry has been multiplied by $(2J + 1)$.

$$P(\cos\theta) = \frac{(2J+1)}{2}\sum_{n=0}^{2J} C_n(J\Omega\mathrm{M})\, P_n(\cos\theta) \qquad (17)$$

where the $P_n(\cos\theta)$ are Legendre polynomials and θ corresponds to the angle between the permanent electric dipole moment vector $\boldsymbol{\mu}$ and the local electric field vector $\boldsymbol{\epsilon}$. The expansion coefficients C_n are determined by projecting the rotational state wave function onto the Legendre polynomials. In the limit of high field, the pure Hund's case a wave functions for $^2\Pi_\Omega$ diatomics are given by the Wigner rotation matrices $\mathbf{D}^J_{M\Omega}$, and the expansion coefficients are conveniently expressed in terms of 3-*j* symbols:[53]

$$C_n(J\Omega M) = (2n+1)(-1)^{M-\Omega}\begin{pmatrix} J & J & \mathrm{n} \\ \Omega & -\Omega & 0 \end{pmatrix}\begin{pmatrix} J & J & \mathrm{n} \\ \mathrm{M} & -M & 0 \end{pmatrix} \qquad (18)$$

In contrast to NO, neither OH nor OD are good Hund's case a molecules, particularly as J increases. To incorporate the mixing of $\Omega = {}^3/_2$ and $\Omega = {}^1/_2$ spin−orbit states of OH (OD), linear combinations of the C_n expansion coefficients were taken using coefficients for the mixed cases from Table 3 as shown below:

$$C_n(J\,\Omega = {}^3/_2\, M) = a_J{}^2 C_n(J\,\Omega = {}^3/_2\, M) + b_J{}^2 C_n(J\,\Omega = {}^1/_2\, M) \qquad (19)$$

$$C_n(J\,\Omega = {}^1/_2\, M) = a_J{}^2 C_n(J\,\Omega = {}^1/_2\, M) + b_J{}^2 C_n(J\,\Omega = {}^3/_2\, M) \qquad (20)$$

where the coefficients a_J and b_J are determined from eq 11. The orientational pdf's produced by this treatment are shown in Figure 7 for several low-lying rotational states of OH and OD.

A problem that remains is to calculate the orientational pdf's at lower field strengths where Λ-doubling effects manifest themselves. In general, the Legendre polynomial expansion coefficients $C_n(\epsilon)$ will be functions of the field strength. This involves the more difficult task of projecting the $|J\Omega MA'\rangle$ and $|J\Omega MA''\rangle$ wave functions onto the Legendre polynomials, a problem we will not address here. It is very straightforward, however, to calculate the $\langle\cos\theta\rangle$ to get a feeling for how the orientational pdf's depend on the field strength. In fact, we have already done this (see Figure 3) since $\mu_{\mathrm{eff}} = \mu\langle\cos\theta\rangle$. Notice the saturation values for OH and OD are different since

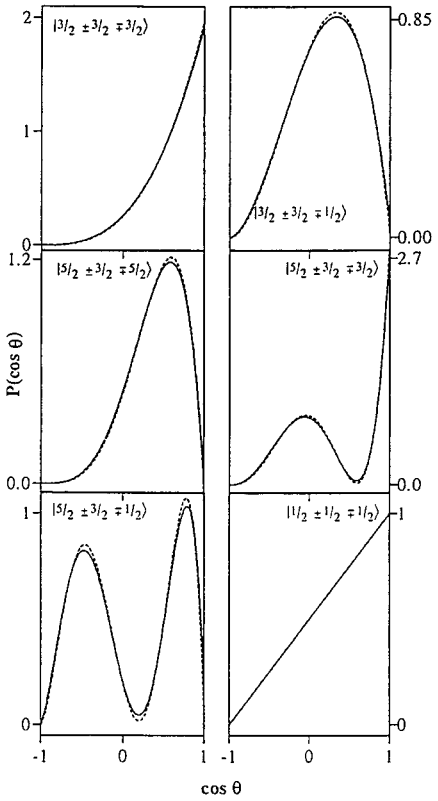

Figure 7. Orientational probability distribution fucntions (pdf's) in the high-field limit for spin−orbit mixed rotational states of OH (solid lines) and OD (dotted lines). The pdf for the $|^1/_2 \pm^1/_2 \mp^1/_2\rangle$ rotational state is pure Hund's case a, and no difference in the pdf for this state exists for OH or OD.

Λ-doublet splittings differ for any J value of the two with the $J = |\Omega| = {}^3/_2$ Λ-doublet splitting being 5.4 times greater in OH than OD.

The two selectable states with the greatest beam intensities are the $|^3/_2 \pm^3/_2 \mp^3/_2\rangle$ and $|^3/_2 \pm^3/_2 \mp^1/_2\rangle$ states. It is clear from Figure 7 that OH/OD radicals selected in the $|^3/_2 \pm^3/_2 \mp^3/_2\rangle$ state are strongly oriented parallel to the local electric field with $\cos\theta$ values near +1 dominating the distribution ($\langle\cos\theta\rangle \approx 0.6$). Imagine a bimolecular scattering experiment where the local electric field vector is directed along the relative velocity vector. Beautiful "heads" (oxygen end) versus "tails" (hydrogen end) steric effect measurements can be made by simply changing the direction of the local electric field vector. The $P(\cos\theta)$ distribution for the $|^3/_2 \pm^3/_2 \mp^1/_2\rangle$ state is qualitatively very

different. For this state there is a node at $\cos\theta = +1$, and the rotational motion of the molecular axis is localized around cos θ values near zero ($\langle\cos\theta\rangle \approx 0.2$). This indicates "side-on" collisions rather than "heads-on" or "tails-on" collisions will dominate. Our ability to isolate these two states provides us with exceptional control over the collision geometry in such scattering experiments.

6. Summary

We have described a new molecular beam apparatus designed to rotationally state-select and orient highly reactive radicals. Radicals are generated in a supersonic corona discharge beam source. This source is particularly well-suited to state-selection by the hexapole focusing technique because radicals are produced in good yield in a molecular beam characterized by low stream velocity and low rotational and translational temperatures. The capabilities of this new instrument have been demonstrated by reporting OH/OD focusing spectra measured with a quadrupole mass spectrometer. Interpretation of these spectra was facilitated by simulations with trajectory calculations that incorporated effects due to Λ-doubling and spin−orbit interactions for the first time. Agreement between experimental and simulated spectra was good, particularly at low hexapole potentials. The Λ-doubling effect was shown to significantly affect the peak positions and widths.

Two rotational states of OH and OD were readily isolated, the $|J\ \pm\Omega\ \mp M_J\rangle = |{}^3/_2\ \pm{}^3/_2\ \mp{}^3/_2\rangle$ and $|{}^3/_2\ \pm{}^3/_2\ \mp{}^1/_2\rangle$ states. Beam flux densities for both exceeded 10^{13} cm^{-2} s^{-1}. The kinetic energy of the hydroxyl radical beams was varied from 0.05 to 0.31 eV by seeding in Ar and He, respectively. The terminal beam velocity was determined by the nozzle temperature. A broader range of energies can be accessed by heating and cooling the nozzle. The orientational probability distribution functions for six selectable states were calculated in the high-field limit including spin−orbit mixing. These demonstrate excellent experimental control over the orientation of the hydroxyl radical axis in the laboratory frame of reference.

Acknowledgment. The authors are grateful for funding received from the NSF NYI Program (Grant No. CHE9457382), the Research Corp., and the University of Utah. We gratefully acknowledge the use of the computer facilities provided by the Utah Supercomputing Institute at the University of Utah. The authors benefited by useful discussions with Professors Michael Morse and Steven Stolte. Construction of the apparatus was facilitated by the technical assistance of Mssrs. Dale Heisler, Ron Jones, Mark Pezel, Dennis Romney, and Mike Scott of the Department of Chemistry at the University of Utah.

References and Notes

(1) Miller, J. A.; Fisk, G. A. *Chem. Eng. News* **1987**, *65*, 22.
(2) Melissas, V. S.; Truhlar, D. G. *J. Chem. Phys.* **1993**, *99*, 1013.
(3) Miyoshi, A.; Yamauchi, N.; Matsui, H. *J. Phys. Chem.* **1996**, *100*, 4893.
(4) Kwok, E. S. C.; Arey, J.; Atkinson, R. *J. Phys. Chem.* **1996**, *100*, 214.
(5) Sekusak, S.; Gusten, H.; Sabljic, A. *J. Phys. Chem.* **1996**, *100*, 6212.
(6) Nanayakkara, A. A.; Balint-Kurti, G. G.; Williams, I. H. *J. Phys. Chem.* **1992**, *96*, 3662.
(7) Hynes, A. J.; Stoker, R. B.; Pounds, A. J.; McKay, T.; Bradshaw, J. D.; Nicovich, J. M.; Wine, P. H. *J. Phys. Chem.* **1995**, *99*, 6967.
(8) Wennberg, P. O.; Cohen, R. C.; Stimpfle, R. M.; Koplow, J. P.; Anderson, J. G.; Salawitch, R. J.; Fahey, D. W.; Woodbridge, E. L.; Keim, E. R.; Gao, R. S.; Webster, C. R.; May, R. D.; Toohey, D. W.; Avallone, L. M.; Proffitt, M. H.; Loewenstein, M.; Podolske, J. R.; Chan, K. R.; Wofsy, S. C. *Science* **1994**, *266*, 398.
(9) Yang, H.; Whitten, J. *Surf. Sci.* **1989**, *223*, 131.
(10) Anton, A. B.; Cadogan, D. C. *J. Vac. Sci. Technol. A* **1991**, *9*, 1890.
(11) Fridell, E.; Elg, A.-P.; Rosén, A.; Kasemo, B. *J. Chem. Phys.* **1995**, *102*, 5827.
(12) Backstrand, K. M.; Hain, T. D.; Weibel, M. A.; Curtiss, T. J. *Surf. Sci.*, submitted for publication.
(13) Fisher, E. R.; Ho, P.; Breiland, W. G.; Buss, R. J. *J. Phys. Chem.* **1993**, *97*, 10287.
(14) Wurps, H.; Spiecker, H.; ter Meulen, J. J.; Andressen, P. *J. Chem. Phys.* **1996**, *105*, 2654.
(15) Fowler, D. R. *Int. Rev. Phys. Chem.* **1995**, *14*, 421.
(16) Alagia, M.; Balucani, N.; Casavecchia, P.; Stranges, D.; Volpi, G. G. *J. Chem. Phys.* **1993**, *98*, 2459.
(17) See for example: Alagia, M.; Balucani, N.; Casavecchia, P.; Stranges, D.; Volpi, G. G.; Clary, D. C.; Kliesch, A.; Werner, H.-J. *Chem. Phys.* **1996**, *207*, 389, and references cited therein.
(18) Zhang, D. H.; Zhang, J. Z. H. *Chem. Phys. Lett.* **1995**, *232*, 370.
(19) Nyman, G.; Clary, D. C. *J. Chem. Phys*. **1994**, *101*, 5756.
(20) Clary, D. C.; Nyman, G.; Hernandez, R. *J. Chem. Phys*. **1994**, *101*, 3704.
(21) Nyman, G. *J. Chem. Phys*. **1996**, *104*, 6154.
(22) Hain, T. D.; Weibel, M. A.; Backstrand, K. M.; Pope, P. E.; Curtiss, T. J. *Chem. Phys. Lett.* **1996**, *262*, 723.
(23) Weibel, M. A.; Hain, T. D.; Curtiss, T. J. *J. Vac. Sci. Technol. A*, in press.
(24) Engelking, P. C. *Rev. Sci. Instrum.* **1986**, *57*, 2274.
(25) Our simulations predict rotational state peak positions in focusing spectra that are systematically ~10% higher than observed experimentally. This occurs for simple symmetric tops (e.g., CH_3Cl, CH_3F, and CF_3H) as well as for the more complicated hydroxyl radical spectra reported here. Due to the sensitivity of the focusing on the hexapole radius r_0 (see eq 5) and the inherent difficulty in aligning a 2 m long hexapole, this discrepancy is most easily corrected by adopting an "effective" value of $r_0 = 9.9$ mm, a strategy adopted previously by Bernstein and co-workers (see, for example, refs 60 and 62). We used $r_0 = 9.9$ mm in our simulations. However, it is also possible the methodology of Chakravorty *et al*. (see ref 34) and Choi (ref 62) that we have used here as well has some defect we do not understand. We are currently working to resolve this issue.
(26) Zeman, H. D. *Rev. Sci. Instrum.* **1977**, *48*, 1079.
(27) Bickes, R. W., Jr.; Newton, K. R.; Herrman, J. M.; Bernstein, R. B. *J. Chem. Phys.* **1976**, *64*, 3648.
(28) This value is an average of references: Ma, C.; Sporleder, C. R.; Bonham, R. A. *Rev. Sci. Instrum.* **1991**, *62*, 909. Stephan, K.; Helm, H.; Märk, T. D. *J. Chem. Phys.* **1980**, *73*, 3763. Wetzel, R. C.; Baiocchi, F. A.; Hayes, T. R.; Freund, R. S. *Phys. Rev. A* **1987**, *35*, 559.
(29) Tarnovsky, V.; Becker, K. Private communication, 1997.
(30) Tarnovsky, V.; Becker, K. *Int. J. Mass Spectrom. Ion Processes*, to be published.
(31) Auerbach, D. J. In *Atomic and Molecular Beam Methods*; Scoles, G., Ed.; Oxford University: New York, 1982; Vol. 1, Chapter 14.
(32) Bernstein, R. B. *Chemical Dynamics via Molecular Beam and Laser Techniques*; Oxford University: New York, 1982; Chapter 3.
(33) Bernstein, R. B. *Chemical Dynamics via Molecular Beam and Laser Techniques*; Oxford University: New York, 1982; Chapter 4.
(34) Chakravorty, K. K.; Parker, D. H.; Bernstein, R. B. *Chem. Phys.* **1982**, *68*, 1.
(35) Gandhi, S. R.; Curtiss, T. J.; Xu, Q.-X.; Choi, S. E.; Bernstein, R. B. *Chem. Phys. Lett.* **1986**, *132*, 6.
(36) Harren, F.; Parker, D. H.; Stolte, S. *Comments At. Mol. Phys.* **1991**, *26*, 109.
(37) Ohoyama, H.; Ogawa, T.; Kasai, T. *J. Phys. Chem.* **1995**, *99*, 13606.
(38) Jalink, H.; Harren, F.; van den Ende, D.; Stolte, S. *Chem. Phys.* **1986**, *108*, 391.
(39) Kuwata, K.; Kasai, T. In *Chemical Dynamics and Kinetics of Small Radicals*; Liu, K., Wagner, A., Eds.; World Scientific: London, 1995; Part II, Chapter 19. Takezaki, M.; Ohoyama, H.; Kasai, T.; Kuwata, K. *Laser Chem.* **1995**, *15*, 113.
(40) Mizushima, M. *Phys. Rev. A* **1972**, *5*, 143.
(41) Meerts, W. L.; Dynamus, A. *Chem. Phys. Lett.* **1973**, *23*, 45.
(42) Dousmanis, G. C.; Sanders, T. M.; Townes, C. H. *Phys. Rev.* **1955**, *100*, 1735.
(43) Meerts, W. L.; Dynamus, A. *Astrophys. J.* **1973**, *180*, L93.
(44) Mizushima, M. *The Theory of Rotating Diatomic Molecules*; Wiley: New York, 1975; p 306.
(45) Huber, K. P.; Herzberg, G. *Molecular Spectra and Molecular Structure IV Constants of Diatomic Molecules*; Van Nostrand Reinhold Company: New York, 1979.
(46) *CRC Handbook of Chemistry and Physics*, 74th ed.; Lide, D. R., Ed.; CRC: Boca Raton, FL, 1993; Section 9.
(47) Kuipers, E. W.; Tenner, M. G.; Kleyn, A. W.; Stolte, S. *Chem. Phys.* **1989**, *138*, 451.
(48) Bernath, P. F.; Brazier, C. R.; Olsen, T.; Hailey, R.; Fernando, W. T. M.; Woods, C.; Hardwick, J. L. *J. Mol. Spectrosc.* **1991**, *147*, 16.
(49) Turner, B. E.; Zuckerman, B. *Astrophys. J.* **1974**, *187*, L59.
(50) Morino, I.; Kawaguchi, K. *J. Mol. Spectrosc.* **1995**, *170*, 172.
(51) Meerts, W. L.; Dynamus, A. *Astrophys. J.* **1974**, *187*, L45.

(52) Saito, M.; Endo, Y.; Takami, M.; Hirota, E. *J. Chem. Phys.***1983**, *78*, 116.
(53) Zare, R. N. *Angular Momentum*; Wiley: New York, 1988; Application 15.
(54) Alexander, M. H.; Andressen, P.; Bacis, R.; Bersohn, R.; Comes, F. J.; Dagdigian, P. J.; Dixon, R. N.; Field, R. N.; Flynn, G. W.; Gericke, K.-H.; Grant, E. R.; Howard, B. J.; Huber, J. R.; King, D. S.; Kinsey, J. L.; Kleinermanns, K.; Rosenwaks, S.; Rothe, E. W.; Shapiro, M.; Simons, J. P.; Vasudev, R.; Weisenfeld, J. R.; Wittig, C.; Zare, R. N. *J. Chem. Phys.* **1988**, *89*, 1749.
(55) Gordy, W.; Cook, R. L. *Microwave Molecular Spectra*; Wiley: New York, 1984; p 32.
(56) Townes, C. H.; Schalow, A. L. *Microwave Spectroscopy*; Dover: New York, 1975; Chapter 10.
(57) Gordy, W.; Cook, R. L. *Microwave Molecular Spectra*; Wiley: New York, 1984; Chapter X.
(58) Jones, E. M.; Brooks, P. R. *J. Chem. Phys.* **1970**, *53*, 55.
(59) Gandhi, S. R.; Xu, Q.-X.; Curtiss, T. J.; Bernstein, R. B. *J. Phys. Chem.* **1987**, *91*, 5437.
(60) Gandhi, S. R.; Bernstein, R. B. *J. Chem. Phys.* **1987**, *87*, 6457.
(61) Mizushima, M. *The Theory of Rotating Diatomic Molecules*; Wiley: New York, 1975; p 117.
(62) Choi, S. E. Ph.D. Thesis, University of California—Los Angeles, 1987.
(63) Schreel, K.; Schleipen, J.; Eppink A.; ter Meulen, J. J. *J. Chem. Phys*. **1993**, *99*, 8713. Schreel, K.; ter Meulen, J. J. *J. Chem. Phys.* **1996**, *105*, 4522.
(64) Parker, D. H.; Bernstein, R. B. *Annu. Rev. Phys. Chem.* **1989**, *40*, 561.
(65) Stolte, S. In *Atomic and Molecular Beam Methods*; Scoles, G., Ed.; Oxford University: New York, 1988; Vol. 1, Chapter 25.
(66) Kuipers, E. W.; Tenner, M. G.; Kleyn, A. W.; Stolte, S. *Phys. Rev. Lett.* **1989**, *62*, 2152.
(67) Curtiss, T. J.; Mackay, R. S.; Bernstein, R. B. *J. Chem. Phys.* **1990**, *93*, 7387.
(68) Choi, S. E.; Bernstein, R. B. *J. Chem. Phys.* **1986**, *85*, 150.
(69) Tenner, M. G.; Kuipers, E. W.; Langhout, W. Y.; Kleyn, A. W.; Nicolasen, G.; Stolte, S. *Surf. Sci.* **1990**, *236*, 151.